Metal Halide Perovskite Surfaces with Mixed A-Site Cations: Atomic Structure and Device Stability

ADVANCED FUNCTIONAL MATERIALS
www.afm-journal.de

Metal Halide Perovskite Surfaces with Mixed A-Site Cations: Atomic Structure and Device Stability

*Jeremy Hieulle, Dae-Yong Son, Afshan Jamshaid, Xin Meng, Collin Stecker, Robin Ohmann, Zonghao Liu, Luis K. Ono, and Yabing Qi**

Mixing cations in the perovskite structure has been shown to improve optoelectronic device performance and stability. In particular, $Cs_xMA_{1-x}PbBr_3$ ($MA = CH_3NH_3$) has been used to build high-efficiency light-emitting diodes. Despite those advantages, little is known about the exact location of the cations in the mixed perovskite film, and how cation distribution affects device properties and stability. By using scanning tunneling microscopy , the exact atomic structure of the mixed cation $Cs_xMA_{1-x}PbBr_3$ perovskite interface is revealed. In addition, X-ray photoelectron spectroscopy, ultraviolet photoemission spectroscopy and inverse photoemission spectroscopy are used to study the stability and electronic properties of the $Cs_xMA_{1-x}PbBr_3$ perovskite film. Partial substitution of MA^+ by Cs^+ induces a modification of the perovskite surface structure, leading to improved device stability is shown. These results provide a better understanding of the key parameters involved in the stability of mixed cation perovskite solar cells.

1. Introduction

Mixed cation $Cs_xMA_{1-x}PbBr_3$ perovskites are good candidates for use in optoelectronic devices.[1–11] The capping of $CsPbBr_3$ perovskite with a MABr passivation layer has led to an external quantum efficiency (EQE) of over 20%.[4] Additionally, Cs incorporation in $MAPbI_3$ and $FAPbI_3$ (FA = formamidinium) perovskites, has been shown to improve the stability and increase power conversion efficiency (PCE) in solar cells.[12–15] Improving solar cells' stability is one of the milestones that could open the path toward the future commercialization of perovskite-based technology.[16–19] Cesium cations have also been used to tune energy level alignment in $MAPbI_3$ to improve charge injection in the electron transport layer (ETL).[20] Cs cations are also largely employed to stabilize the black alpha-phase of $FAPbI_3$ perovskite.[21] More recently, Cs cation has been used to control halide segregation in the perovskite film.[22] Another study reported that doping the $MAPbI_3$ perovskite with Cs cations greatly increased the carrier diffusion length in the perovskite films, which was successfully employed to design a highly efficient solar module.[23] As a consequence, Cs is a good candidate for building efficient[24,25] and stable[26–29] mixed cation perovskite devices.

Cation distribution has been shown to drastically impact the optical properties of the perovskite active layer, such as the local work function and absorbance.[30] The modification in the local optical properties of the perovskite film is expected to have a strong influence on the final device performance. However, only a few studies have been performed to determine the distribution of the cations in mixed perovskites and their influence on material properties.[31–33] A better understanding of the relation between the perovskite electronic properties and local cation distribution could open new routes for device engineering.

Scanning tunneling microscopy (STM) is a powerful technique for determining local ion distribution at the surface of perovskite materials with atomic-scale precision.[34–39] Additionally, ultraviolet photoemission spectroscopy (UPS) and inverse photoemission spectroscopy (IPES) are useful tools to reveal the electronic structure of perovskite materials[29,40,41].

Here, by combining STM, UPS, and IPES, we determine the exact distribution of the cations in $Cs_xMA_{1-x}PbBr_3$ perovskite films at the atomic scale and correlate it to the material's electronic properties and stability. We show that partial substitution of the MA cation by Cs in $MAPbBr_3$ leads to improved stability of a full device solar cell, without strongly impacting its electronic properties and performance. Our research aims to provide the accurate atomic structure of the perovskite surface to better predict and simulate interfacial properties in the device and unravel the parameters influencing device stability.

2. Results and Discussion

To determine the influence of MA and Cs cation mixing on the perovskite electronic properties and stability, we investigated

J. Hieulle, D.-Y. Son, A. Jamshaid, C. Stecker, R. Ohmann, Z. Liu, L. K. Ono, Y. Qi
Energy Materials and Surface Sciences Unit (EMSSU)
Okinawa Institute of Science and Technology Graduate University (OIST)
1919-1 Tancha, Onna-son, Okinawa 904-0495, Japan
E-mail: Yabing.Qi@OIST.jp
X. Meng, Z. Liu
Wuhan National Laboratory for Optoelectronics
Huazhong University of Science and Technology
Wuhan 430074, China
The ORCID identification number(s) for the author(s) of this article can be found under https://doi.org/10.1002/adfm.202211097.

DOI: 10.1002/adfm.202211097

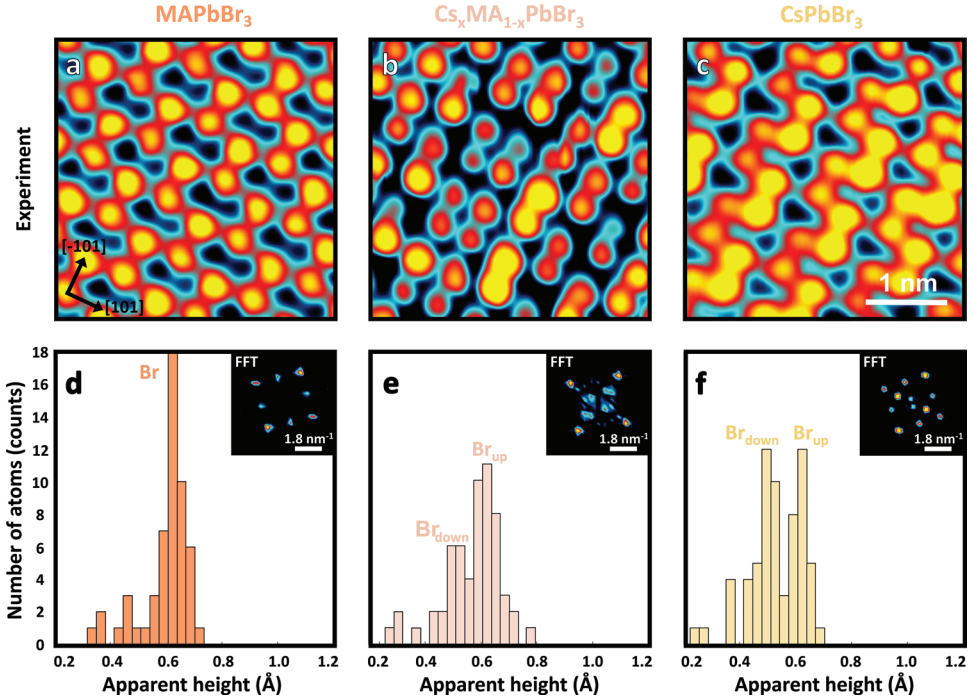

Figure 1. Cation mixing at the perovskite surface. a–c) Scanning tunneling microscopy images of $MAPbBr_3$ (a), $Cs_xMA_{1-x}PbBr_3$ (b) and $CsPbBr_3$ (c) perovskite surfaces. Image parameters: (a) sample bias = +1.3 V, tunneling current = 80 pA; (b) −2.7 V, 20 pA; (c) +2.0 V, 100 pA; Image size: (a–c) 3.5 × 3.5 nm^2. d–f) Histograms of the apparent height distribution of local maxima (ions). The insets in d–f represent the Fourier transform extracted from the STM images in a–c.

the $Cs_xMA_{1-x}PbBr_3$ perovskite film. Here, the mixed cation $Cs_xMA_{1-x}PbBr_3$ was grown by thermal evaporation of CsBr on a pre-formed $MAPbBr_3$ film (see methods). The $MAPbBr_3$ film was obtained by simultaneous evaporation of MABr and $PbBr_2$ precursors on an Au(111) substrate kept at 132 K, following a previously reported method[42].

Figure. 1 shows the comparison between the newly formed $Cs_xMA_{1-x}PbBr_3$ film with the surface atomic structure of pristine $CsPbBr_3$ and $MAPbBr_3$ perovskites.[34,37,43] A characteristic feature that the three surface structures have in common, is the slight displacement of neighboring Br ions toward each other to form bromine pairs. For $MAPbBr_3$, the Br pairs are equally spaced and appear with the same brightness in the STM images (Figure 1a), in contrast to what we observed for $CsPbBr_3$ (Figure 1c). The long-range order induced by the alternation of the dark and bright Br rows in $CsPbBr_3$ leads to the appearance of additional peaks at a low *k*-value in the Fourier transform of the STM image (inset in Figure 1f). Those peaks are not observed for $MAPbBr_3$ perovskite (inset, Figure 1d). For the mixed cation perovskite case, the surface structure exhibits characteristic features of both $CsPbBr_3$ and $MAPbBr_3$ perovskites (Figure 1b, inset in 1e). First, a pair motif can be seen in the $Cs_xMA_{1-x}PbBr_3$ film, even though the structure seems to be less periodic than that of the pristine perovskites. Moreover, several different heights can be observed in the mixed-cation perovskite film. This observation suggests that the additional Cs cations are modifying the vertical position of the neighboring Br ions.

The distributions of the distinct apparent heights observed for the three perovskite films are presented in Figure 1d–f. For $MAPbBr_3$ a single peak is observed at 0.6 Å associated with the bromine ions of the MABr top-layer (Figure 1d). For $CsPbBr_3$, two main peaks with similar occurrences can be observed at 0.5 and 0.6 Å, corresponding to the dark and bright bromine rows, respectively (Figure 1f). In contrast, for the mixed cations $Cs_xMA_{1-x}PbBr_3$ film, a small peak is observed at 0.5 Å and a strong peak is seen at 0.6 Å height (Figure 1e). The height distribution observed for the mixed cation seems to be an intermediate state between the distribution of pristine $CsPbBr_3$ and $MAPbBr_3$ perovskites.

In the following, we take a closer look at the atomic structure of the mixed cation perovskite surface. A change in the lateral position of the bromine pairs is observed at the surface of the mixed cation perovskite. As shown in **Figure 2**a, a new "side-by-side" structure appears in the mixed $Cs_xMA_{1-x}PbBr_3$ film, where some of the neighboring Br pairs are packed in a nearly square fashion (indicated by white rectangles). This packing of the Br pairs in the mixed cation perovskite can be explained by the substitution of the polar MA molecules by non-polar Cs cations. A Cs incorporation ratio of x = 0.13 was determined by X-ray photoelectron spectroscopy (XPS) (Figure S1, Supporting Information). The replacement of a polar species by a non-polar Cs directly affects the coupling between the neighboring Br^- pairs. Therefore, we attribute the usual shifted Br^- pairs to MA^+ rich region (similar to $MAPbBr_3$), and the side-by-side Br^- pairs to Cs^+ rich region in the mixed $Cs_xMA_{1-x}PbBr_3$ perovskite (Figure 2b).

Considering these observations, we constructed a tentative model of the surface atomic structure of mixed cation perovskite. The rectangular unit cell of this model is presented in Figure 2c. The lattice parameters are E = 15.7, F = 10.0 Å. The motif of the mixed structure is composed of 2 Cs, 4 MA cations,

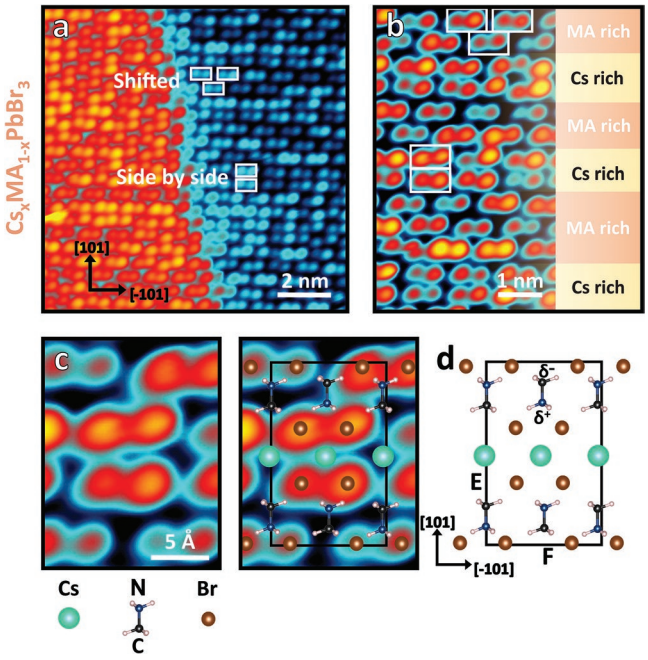

Figure 2. Mixed cations surface structure. a) Large area STM image and b,c) zoom-in images of mixed cation $Cs_xMA_{1-x}PbBr_3$ perovskite. d) Tentative model of the surface reconstruction of the mixed $Cs_xMA_{1-x}PbBr_3$ perovskite. The middle bottom panel corresponds to the overlay of (c,d). Image parameters: (a–c) sample bias = –1.5 V, tunneling current = 20 pA; Image size: (a) 11.3 × 11.3; (b) 4.0 × 6.7 nm^2 (c) 1.5 × 2.0 nm^2. In the model, white, blue, black, brown, and green balls denote, respectively, hydrogen, nitrogen, carbon, bromine, and cesium atoms. The red and blue colors in the STM image in (a) correspond to two different atomic steps (red = higher step, blue lower step).

and 6 Br anions (Figure 2d). In this model, the Br^- pairs are surrounded by at least one MA^+ cation. The N-terminated side of the MA molecules with a partial positive charge (δ^+) is pointing toward the Br^- pairs, according to what we previously demonstrated[34] for pristine $MAPbBr_3$. The side-by-side packing of the Br^- pairs is made possible by the centrosymmetric nature of the Cs^+ cations; in contrast, the MA^+ cations exhibit a dipole that moves apart Br^- at the negative termination and attracts Br^- at the positive termination. Such changes in surface reconstruction as a function of local cation distribution might induce local compressive/tensile strains that in turn affect the local electronic properties through band-bending[44].

In addition to their distinct surface reconstructions, strong differences were found in the electronic properties of the three perovskite films. The UPS and IPES results obtained on $CsPbBr_3$, $Cs_xMA_{1-x}PbBr_3$, and $MAPbBr_3$ are depicted in **Figure 3**. The positions of the valence band maximum (VBM) and conduction band minimum (CBM) were found to be shifted down for $CsPbBr_3$ (VBM = –1.86 eV; CBM = +0.36 eV; E_g = 2.22 eV), as compared to $MAPbBr_3$ perovskite (VBM = – 0.56 eV; CBM = +1.85 eV; E_g = 2.41 eV). Such changes in the VBM and CBM positions would alter the charge transfer properties at the interface of the perovskite film. The bandgaps (E_g) extracted from the energy positions difference of the VBM and CBM are consistent with previous reports in the literature.[45,46] Interestingly, a downward band bending was found for the $Cs_xMA_{1-x}PbBr_3$ mixed cation film as compared to $MAPbBr_3$, even at low Cs incorporation ratio (e.g., VBM = – 0.57 eV; CBM = +1.70 eV; E_g = 2.27 eV). This specific behavior should be considered when engineering optoelectronic devices based on mixed cation perovskites.

Only a small difference is observed between the work function of $MAPbBr_3$ (4.6 ± 0.2 eV) and $Cs_{0.13}MA_{0.87}PbBr_3$ (4.7 ± 0.2 eV) perovskites, which is within the experimental error (Figure 3), while the work function of $CsPbBr_3$ was found to be much lower (3.6 ± 0.2 eV). It is worth noting that similar work function values were reported previously[27].

To investigate the stability of the perovskite materials, we performed XPS on a half-solar cell architecture. First, the $MAPbBr_3$, $Cs_{0.13}MA_{0.87}PbBr_3$, and $CsPbBr_3$ films with a thickness of ≈300 nm were spun on a TiO_2/FTO/glass substrate

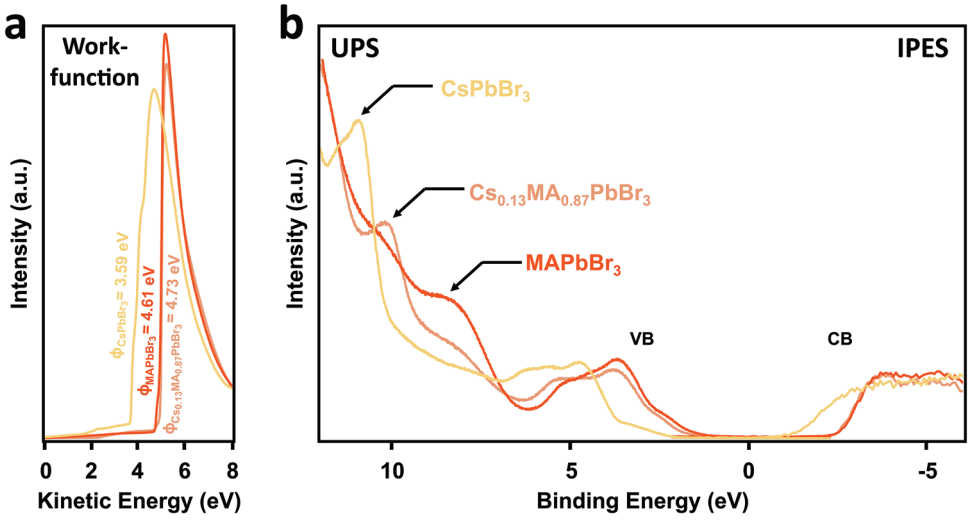

Figure 3. Comparison of work function and band onsets of the mixed cation perovskite and corresponding pristine perovskites. a) Work function is measured by ultraviolet photoemission spectroscopy (UPS). b) Valence band maximum (VBM) and conduction band minimum (CBM) were obtained on pristine $MAPbBr_3$, $CsPbBr_3$, and mixed cation $Cs_{0.13}MA_{0.87}PbBr_3$ perovskites by UPS and inverse photoemission spectroscopy spectra (IPES).

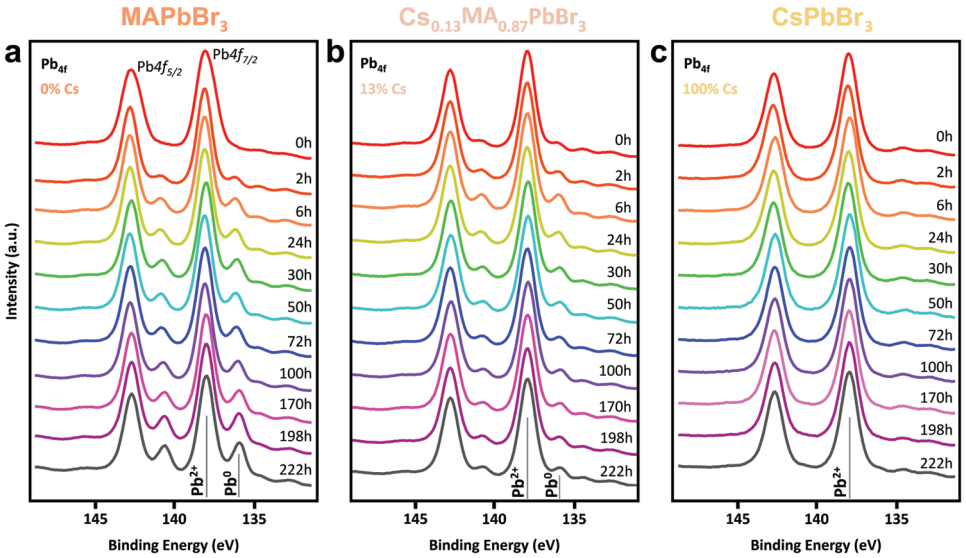

Figure 4. Stability improvement via Cs incorporation. a–c) Time evolution of the Pb 4f spectra obtained by X-ray photoelectron spectroscopy (XPS) on a device architecture (a) without the addition of Cs, (b) with 13% of Cs, and (c) with 100% Cs.

(FTO is fluorine-doped tin oxide; see the Experimental Section), which resembles half (up to the perovskite layer) of a standard perovskite solar cell structure. The half-cell architectures were then transferred into the UHV system to investigate their degradation by XPS (**Figure 4**). First, the evolution of the Pb *4f* spectra was monitored for pristine $MAPbBr_3$ without any Cs content. Figure 4a shows that initially (at $T = 0$ h) the spectrum is composed of only two peaks at 137.9 and 142.8 eV, attributed to the spin–orbit split Pb $4f_{7/2}$ and Pb $4f_{5/2}$ peaks and referred to as Pb^{2+}. After only 2 h, additional peaks appear at lower binding energies corresponding to the lower oxidation of the Pb^0 state. Such a state is associated with the deterioration of the perovskite film[43,47,48].

In the present study, we measured the time evolution of the Pb^0 feature to track the degradation of the perovskite films. As time passes, the intensity of the Pb^0 peak increases for the pristine $MAPbBr_3$ film (Figure 4a), showing a strong and progressive degradation of the perovskite material. For the $Cs_{0.13}MA_{0.87}PbBr_3$ film, a small Pb^0 peak can be observed, however, its intensity is greatly reduced in comparison with $MAPbBr_3$ and after an initial increase, its intensity does not increase over time (Figure 4b). Therefore, a clear reduction of the perovskite degradation is observed when substituting 13% of the MA cations with Cs ($Cs_{0.13}MA_{0.87}PbBr_3$). In contrast, for the $CsPbBr_3$ perovskite film (i.e., with 100% Cs), no Pb^0 peak was observed[49] even after 222 h. The time evolution profile of the Pb^{2+} peak intensity for the three perovskites also confirms quantitatively the improved stability (Figure S2, Supporting Information). It is important to point out that STM is mainly a surface-sensitive technique, and XPS can typically probe up to top 10 nm of the sample (near-surface region). Due to such experimental limitations, it is difficult to provide information about the vertical distribution of the Pb^0 species. However, in one of our previous studies, DFT calculation results suggest that MABr vacancy defects are energetically favored at the topmost surface as compared to the bulk. Therefore, once MABr vacancies are created due to the perovskite degradation, those vacancies will migrate toward the surface leading to a higher content of Pb^0 at the surface as compared to the bulk[37].

Similarly, a higher stability of Cs-containing absorbers was observed in photoluminescence (PL) measurements performed in dry N_2 environment (Figure S3, Supporting Information). Among these three samples, it was found that $Cs_{0.13}MA_{0.87}PbBr_3$ retained a much higher PL intensity under continuous laser illumination, suggesting a higher stability of this material with respect to the pristine $MAPbBr_3$.

Previous reports[45] have demonstrated that the non-centrosymmetric nature of the MA^+ cations induces a distortion of the perovskite's octahedrons. Such distortion can reduce the Pb—Br σ-interaction, and induce a Pb—Br bond length alternation. In contrast, filling the perovskite cage with the centrosymmetric Cs^+ cation allows a perfect 90° Br—Pb—Br angle, with equidistant Pb—Br bond length. Therefore, the increase of stability of the mixed cation perovskite film under the incorporation of Cs cation can be understood as a result of the change in the surface structure presented earlier (Figure 2), where the "side-by-side" areas originate from the reduction of the octahedrons' distortion, enabling a stronger Pb—Br σ-interaction.

To further investigate this increase in stability after Cs incorporation, we performed stability measurements on full solar cell devices using $MAPbBr_3$, $Cs_{0.13}MA_{0.87}PbBr_3$, and $CsPbBr_3$ as photoactive materials (**Figure 5**). The perovskite materials used in the devices were made by solution processing following a one-step deposition method[50,51] (see Experimental Section). The same device architecture was used for the three different absorbers, in order to assess the intrinsic stability of the perovskite films. The photovoltaic performance of each cell was measured under one sun (100 mW cm^{-2}) illumination condition (Figure 5a). Power conversion efficiencies (PCEs) of 4.56%, 4.38%, and 2.78% were obtained for the $MAPbBr_3$, $Cs_{0.13}MA_{0.87}PbBr_3$, and $CsPbBr_3$ films, respectively. The short-circuit current densities (J_{sc}), open-circuit voltages (V_{oc}), and

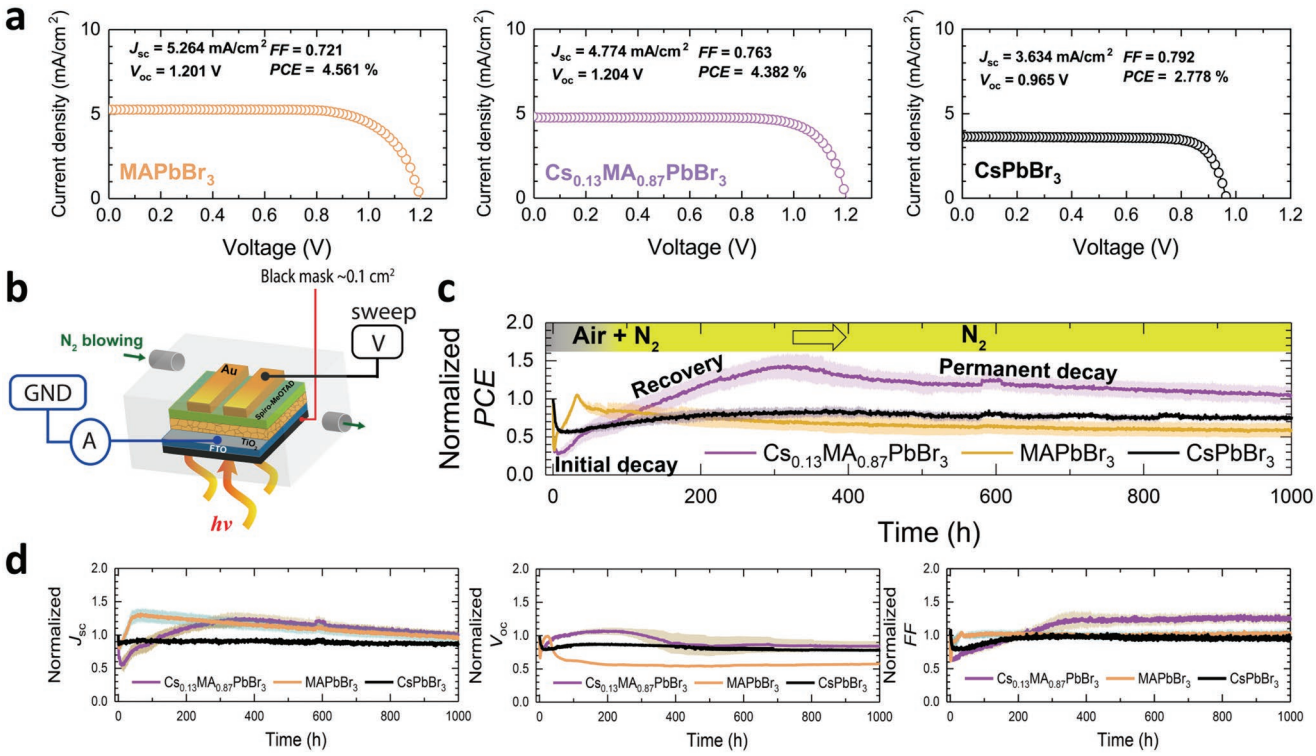

Figure 5. Device performance and stability. a) Current density (J)–voltage (V) curves of perovskite solar cells employing $MAPbBr_3$, $Cs_{0.13}MA_{0.87}PbBr_3$, and $CsPbBr_3$ perovskite films on FTO/c-TiO_2/mp-TiO_2/PSK/spiro-MeOTAD/Au, measured under AM 1.5G one sun illumination condition (100 mW cm^{-2}). The aperture mask area was 0.09 cm^2. b) Schematic configuration of stability measurement in open-circuit condition. The normalized stability of c) PCE, d) J_{sc}, V_{oc}, and FF. $MAPbBr_3$ shows an initial decay for 90 min and recovery to the initial PCE in 32 h. Then, the PCE shows an irreversible decay reaching 58% after 1000 h. The $CsPbBr_3$ solar cell shows a fast decrease in PCE during the first 20 h followed by recovery to 85% in 368 h and maintained 74% at 1000 h. The mixed $Cs_{0.13}MA_{0.87}PbBr_3$ solar cell shows an initial decay to 27% in the first 7 h and recovery attaining 140% in 318 h. Subsequently, it maintained ≈103% after 1000 h.

fill factors (FF) of each cell are presented in Figure 5a. A 10% decrease in the current density is observed after the incorporation of a relatively small amount of Cs (≈13%). Such modification of the current density might be related to the inhomogeneous cation distribution observed in the $Cs_{0.13}MA_{0.87}PbBr_3$ film (Figure 2) inducing local compressive/tensile strain and consequently, band bending that affects the charge transfer dynamics[44].

The stability profile (Figure 5) was recorded under open-circuit and continuous illumination conditions. During the measurements, the solar cells were maintained in an inert environment by flowing N_2 gas in a small transparent chamber (Figure 5b). It is important to note that local heating of the cell was induced by the Xenon lamp used in the experiment (≈35 °C). The results of the stability measurements are depicted in Figure 5c,d.

Several studies reported that reversible decay could be seen in perovskite solar cells.[52,53] Here, we observed those reversible decays in all the samples examined in our experiment. The inflection points at which the stability curves toggle between reversible decay and permanent decay were found at different times for each perovskite material. For $MAPbBr_3$, the inflection point appeared after only 32 h, while the inflexion point appeared after 318 h for mixed $Cs_{0.13}MA_{0.87}PbBr_3$ and 368 h for $CsPbBr_3$ (Figure 5c).

The electric field used in the J–V measurement may induce strong ion migration that affects the stability of the perovskite material and the decay evolution in the stability profiles. Distinct speeds for cation and anion migration were reported in the literature, which could potentially be responsible for the initial decay and subsequent recovery observed here.[54] Additionally, as shown in the previous studies,[13,27,55–58] it is well known that the Cs-incorporated perovskites are less sensitive to thermal stress, humidity, and oxygen than Cs-free perovskite due to the reduction of vacancy formation via strain relaxation.

In our present study, we also show that the incorporation of a small amount of Cs led to better preservation of the open-circuit voltage than pure $MAPbBr_3$ (Figure 5d; Figure S4, Supporting Information). Interestingly, our results show that the slope of permanent decay of Cs incorporated perovskites was significantly reduced (e.g., slower degradation). Also, the PCE recovery after the initial loss was found to be stronger for $Cs_{0.13}MA_{0.87}PbBr_3$ compared to pristine $MAPbBr_3$ and $CsPbBr_3$ perovskites.

Reversible and permanent losses induced by ion migration through vacancies were previously observed when an electric field is applied.[52,53] Here, we measured under open-circuit conditions and could also observe a recovery under continuous illumination. This reversible phenomenon could be a result of ion redistribution taking place after photo-induced structural

changes.[59–63] Recently, Yu and co-workers correlated the light-soaking phenomenon with ion migration.[64] They attributed the increase in PCE to the photovoltage under continuous light illumination, which leads to the movement of ions within the perovskite film increasing charge extraction. Interestingly, the introduction of Cs^+ reduced the density of accumulated mobile ions at the interface demonstrating that the light-soaking phenomenon in the Cs^+-doped device is suppressed. The light-soaking phenomenon on $CsPbI_3$ was also observed to lead to the enhancement in photovoltaic performance due to the neutralization of trap states by the mobile ions.[65] Moreover, it was reported that the energy barrier for ions to migrate is reduced under illumination for MA-based perovskite, while it is rather unaffected for $CsPbX_3$ (X = I, Br).[66] Such findings could explain why we observed a slower decay response for the mixed cation $Cs_{0.13}MA_{0.87}PbBr_3$ perovskite in comparison to pristine $MAPbBr_3$, due to a slower ion migration process under the light. Additional alternatives have been proposed such as the self-healing behavior ascribed to the conversion of decomposed products to perovskite.[47,67] As discussed above, further investigations of the microscopic origins are needed to better understand the light-soaking phenomena in perovskite films and solar cells.[64] Our results provide valuable insights for further engineering of stable perovskite devices via cation mixing and Cs incorporation.

3. Conclusion

In this study, using scanning tunneling microscopy (STM), we determine for the first time the atomic surface structure of mixed cation $Cs_xMA_{1-x}PbBr_3$ perovskite in real space at the atomic scale. The surface of the mixed cation perovskite consists of the alternation of Cs rich and MA rich regions, leading to neighboring Br pairs packed either side-by-side or shifted. The change in the packing of Br pairs most probably results from a reduction of the perovskite octahedral distortion that is usually observed in pure MA-based-perovskite. As a consequence, and as predicted in previous theoretical works, a stronger Pb—Br σ-interaction is established, thus leading to enhanced stability of the perovskite film. Our stability measurements on half- and full- solar cell devices confirm the higher stability of the mixed cations $Cs_xMA_{1-x}PbBr_3$ as compared to pristine $MAPbBr_3$. A slower ion migration process for Cs cations compared to the dipolar MA cations could also be partly responsible for the slower decay and higher stability observed here for $Cs_xMA_{1-x}PbBr_3$ devices. By performing ultraviolet and inverse photoemission spectroscopy measurements, we confirm that the valence and conduction band onsets, as well as the work function of $Cs_xMA_{1-x}PbBr_3$, are very similar to those measured on pristine $MAPbBr_3$ (at a low Cs concentration x < 15%). The improved stability of the perovskite material after Cs incorporation in $MAPbBr_3$, accompanied by minor electronic band modifications, opens up new avenues for the development of stable and efficient optoelectronic devices. Our findings also establish new foundations for more accurate band structure calculations based on the exact surface atomic structure of the mixed cations $Cs_xMA_{1-x}PbBr_3$ perovskite. More accurate band structure calculations are expected to lead to better predictions of the interfacial properties of the perovskite materials with other layers in a device architecture, which will open the way to better device engineering.

4. Experimental section

Surface Characterization: The perovskite films were grown on an Au(111) single crystal using dual-source evaporation, following a previously reported method in the literature.[42] Vacuum deposition techniques have been shown to produce perovskite devices with similar power conversion efficiency to solution-processed material.[63,66,68] The use of the vacuum deposition technique ensures the sample's cleanliness for atomically precise characterization with scanning tunneling microscopy. The gold sample was cleaned in an ultrahigh vacuum environment ($\approx 1 \times 10^{-9}$ torr) with several cycles of Ar^+ sputtering followed by subsequent annealing at 773 K for 5 min. $CsPbBr_3$ perovskite was obtained by simultaneous evaporation of CsBr and $PbBr_2$ precursor molecules at 670 and 515 K, respectively, on the Au(111) sample, and kept at 132 K, for a deposition time of 5 min. Similarly, $MAPbBr_3$ was obtained by the co-deposition of MABr and $PbBr_2$ molecules at 364 and 496 K, respectively, for 5 min. During deposition, the gold surface was kept at 132 K to ensure the adhesion of the methyl-ammonium compound. Mixed cations $Cs_xMA_{1-x}PbBr_3$ perovskite was obtained by sublimating CsBr on the $MAPbBr_3$ film from a Knudsen cell held at 670 K, for 3 min. During sublimation, the sample was kept at room temperature. Low-temperature scanning tunneling microscopy (LT-STM, Scienta Omicron GmbH) was used to characterize the atomic-scale structures of the different perovskite ultra-thin films. All STM measurements were performed at 5 K. A cut Pt/Ir tip was used to acquire the STM images. The bias voltage was applied to the sample. X-ray photoelectron spectroscopy and ultraviolet photoemission spectroscopy (XPS and UPS: Scienta Omicron GmbH) were performed in the same ultra-high vacuum (UHV) setup as the STM measurements. Inverse photoemission spectroscopy (IPES: ALS Technology Co., Ltd.) measurements were conducted in a separated vacuum system with the sample transfer conducted using a vacuum suitcase (Ferrovac GmbH), which prevents contamination from the air.

Solar Cell Fabrication: The patterned FTO glass (Opvtech, 8 Ω^{-2}) was cleaned with detergent and DI water and sonicated with ethanol in an ultrasonic bath for 20 min. Substrates underwent UV-Ozone treatment for 15 min before use. The 80 nm TiO_2 compact (c-TiO_2) layer was deposited via spray pyrolysis at 480 °C from a precursor solution of 2 g of titanium diisopropoxide bis(acetylacetonate) (75 wt% in isopropanol, Sigma–Aldrich) in 1 g of 1-butanol (99.8%, Sigma–Aldrich). The mesoporous TiO_2 (mp-TiO_2) layer with 50 nm thickness was deposited by spin coating at 2000 rpm for 20 s (acceleration was 500 rpm s^{-1}) using the diluted TiO_2 solution in 1-butanol. Then, the substrate was annealed at 550 °C for 30 min. The precursor solution of $MAPbBr_3$ was prepared by mixing 0.367 g of $PbBr_2$ (TCI) and 0.112 g MABr (Methylammonium bromide, Dyesol) in 0.37 mL of DMF with 0.225 mL of DMSO at 60°C, for $Cs_{0.13}MA_{0.87}PbBr_3$, 0.367 g of $PbBr_2$ (TCI), 0.0277 g of CsBr (Sigma–Aldrich, 99.999% trace metal basis) and 0.0974 g of MABr were dissolved in 0.37 mL of DMF (N, N-Dimethylformamide, anhydrous 99.8%) with 0.225 mL of DMSO (Dimethyl Sulfoxide, Sigma Aldrich anhydrous ≥ 99.9%) at 60 °C and for $CsPbBr_3$ 0.58 g of $CsPbBr_3$ powder was dissolved in 1 mL of DMSO. The prepared solutions were spin-coated on the mp-TiO_2 substrate (pre-heated at 75 °C for $CsPbBr_3$ only) at 4000 rpm for 20 s and 0.3 mL of diethyl ether (0.1 mL of toluene for $CsPbBr_3$) was poured when 10 s remained. Then, it was dried on a hot plate at 100 °C (130 °C for $Cs_{0.13}MA_{0.87}PbBr_3$ and 260 °C for $CsPbBr_3$) for 20 min. For the hole transport layer, the 20 µL of 2,2',7,7'-tetrakis(N,N-di-p-methoxyphenyl-amine)-9,9'-spirobifluorene (spiro-MeOTAD) solution, containing of 0.1 g of spiro-MeOTAD (Merck), 39 µL of 4-tert-butyl pyridine (98%, Sigma–Aldrich) and 23 µL of lithium bis(trifluoromethane sulfonyl) imide (Li-TFSI) solution (540 mg Li-TSFI in 1 mL of acetonitrile (99.8%, Sigma Aldrich) in 1.1 mL of chlorobenzene), was spin-coated

on the perovskite layer at 4000 rpm for 30 s. Finally, the Au (80 nm) electrode was evaporated by using a thermal evaporator.

Preparation of $CsPbBr_3$ Powder: The $CsPbBr_3$ powder was synthesized by reacting $PbBr_2$ (TCI) and Cs_2CO_3 in HBr (Sigma Aldrich, 48 wt% in $H_2O \geq 99.99\%$). 3.67 g of $PbBr_2$ was dissolved in 10 mL of HBr solution, during stirring 1.63 g of Cs_2CO_3 (Sigma, 99.995% trace metal basis) was slowly added into the solution. After overnight stirring, the orange-colored precipitation was washed with diethyl ether and isopropanol several times. Then, it was dried at 60 °C for 4 h in a vacuum chamber.

Device Characterizations: Current density–voltage (*J–V*) curves were measured under AM 1.5G one sun (100 mW cm^{-2}) illumination using a solar simulator (Oriel Sol 1A, class ABB) equipped with a 450 W Xenon lamp (Newport 6280NS) and a Keithley 2420 source meter. The light intensity was adjusted by NREL-calibrated Si solar cell (Oriel Instruments Model 91 150 V). The device was covered with a metal mask with an aperture area of 0.09 cm^2. The stability measurement was recorded under continuous illumination (100 mW cm^{-2}) and N_2 flowing system (RH≈5%). Stability measurement (in open-circuit condition) was automatically conducted by voltage sweep from negative to positive (forward scan) and positive to negative (reverse direction) directions every 30 min controlled by homemade LabVIEW code. The temperature was maintained at 35 °C induced by a Xenon lamp.

Photoluminescence Measurements: The perovskite/glass sample fabrication details for in situ PL measurements are similar to the perovskite deposition details for device fabrication (up to the perovskite absorber, half-cell). The in situ PL measurements were obtained by a home-built setup utilizing the ProSp-Micro-MVIS microspectroscopy system (Hangzhou SPL Photonics Co., Ltd.). The samples were excited with a 405 nm laser and the data was collected by a QE-Pro monochromator from Ocean Optics. The PL measurements were performed in a nitrogen-filled chamber.

Supporting Information

Supporting Information is available from the Wiley Online Library or from the author.

Acknowledgements

This work was supported by funding from the Energy Materials and Surface Sciences Unit of the Okinawa Institute of Science and Technology Graduate University, the OIST R&D Cluster Research Program, the OIST Proof of Concept (POC) Program, and JST A-STEP grant number JPMJTM20HS, Japan. The authors thank the OIST Micro/Nanofabrication Section and Imaging Section for their support. The authors would like to thank Prof. Guangda Niu for the fruitful discussion.

Conflict of Interest

The authors declare no conflict of interest.

Data Availability Statement

The data that support the findings of this study are available from the corresponding author upon reasonable request.

Keywords

atomic structures, mixed cations, perovskites, scanning tunneling microscopy, X-ray photoelectron spectroscopy

Received: September 24, 2022
Revised: November 12, 2022
Published online: December 29, 2022

[1] J. Song, J. Li, X. Li, L. Xu, Y. Dong, H. Zeng, *Adv. Mater.* **2015**, *27*, 7162.
[2] L. Zhang, X. Yang, Q. Jiang, P. Wang, Z. Yin, X. Zhang, H. Tan, Y. Yang, M. Wei, B. R. Sutherland, E. H. Sargent, J. You, *Nat. Commun.* **2017**, *8*, 15640.
[3] D. P. McMeekin, G. Sadoughi, W. Rehman, G. E. Eperon, M. Saliba, M. T. Hörantner, A. Haghighirad, N. Sakai, L. Korte, B. Rech, M. B. Johnston, L. M. Herz, H. J. Snaith, *Science* **2016**, *351*, 151.
[4] K. Lin, J. Xing, L. N. Quan, F. Pelayo García de Arquer, X. Gong, J. Lu, L. Xie, W. Zhao, D. Zhang, C. Yan, W. Li, X. Liu, Y. Lu, J. Kirman, E. H. Sargent, Q. Xiong, Z. Wei, *Nature* **2018**, *562*, 245.
[5] J. Li, P. Du, S. Li, J. Liu, M. Zhu, Z. Tan, M. Hu, J. Luo, D. Guo, L. Ma, Z. Nie, Y. Ma, L. Gao, G. Niu, J. Tang, *Adv. Funct. Mater.* **2019**, *29*, 1903607.
[6] W. Pan, B. Yang, G. Niu, K.-H. Xue, X. Du, L. Yin, M. Zhang, H. Wu, X.-S. Miao, J. Tang, *Adv. Mater.* **2019**, *31*, 1904405.
[7] G. Tong, L. K. Ono, Y. B. Qi, *Energy Technol.* **2019**, *8*, 1900961.
[8] G. Tong, T. Chen, H. Li, L. Qiu, Z. Liu, Y. Dang, W. Song, L. K. Ono, Y. Jiang, Y. B. Qi, *Nano Energy* **2019**, *65*, 104015.
[9] M. Jiang, Z. Hu, Z. Liu, Z. Wu, L. K. Ono, Y. B. Qi, *ACS Energy Lett.* **2019**, *4*, 2731.
[10] T. Chen, G. Tong, E. Xu, H. Li, P. Li, Z. Zhu, J. Tang, Y. B. Qi, Y. Jiang, *J. Mater. Chem. A* **2019**, *7*, 20597.
[11] G. Tong, T. Chen, H. Li, W. Song, Y. Chang, J. Liu, L. Yu, J. Xu, Y. B. Qi, Y. Jiang, *Sol. RRL* **2019**, *3*, 1900030.
[12] R. G. Niemann, L. Gouda, J. Hu, S. Tirosh, R. Gottesman, P. J. Cameron, A. Zaban, *J. Mater. Chem. A* **2016**, *4*, 17819.
[13] J.-W. Lee, D.-H. Kim, H.-S. Kim, S.-W. Seo, S. M. Cho, N.-G. Park, *Adv. Energy Mater.* **2015**, *5*, 1501310.
[14] Y. Jiang, M. R. Leyden, L. Qiu, S. Wang, L. K. Ono, Z. Wu, E. J. Juarez-Perez, Y. B. Qi, *Adv. Funct. Mater.* **2018**, *28*, 1703835.
[15] L. Qiu, Z. Liu, L. K. Ono, Y. Jiang, D.-Y. Son, Z. Hawash, S. He, Y. B. Qi, *Adv. Funct. Mater.* **2018**, *29*, 1806779.
[16] S.-Y. Kim, S.-J. Cho, S.-E. Byeon, X. He, H.-J. Yoon, *Adv. Energy Mater.* **2020**, *10*, 2002606.
[17] J.-Y. Lee, S.-Y. Kim, H.-J. Yoon, *Adv. Opt. Mater.* **2021**, *10*, 2101361.
[18] G. Tumen-Ulzii, T. Matsushima, C. Adachi, *Energy Fuels* **2021**, *35*, 18915.
[19] R. Wang, M. Mujahid, Y. Duan, Z.-K. Wang, J. Xue, Y. Yang, *Adv. Funct. Mater.* **2019**, *29*, 1808843.
[20] H. Choi, J. Jeong, H.-B. Kim, S. Kim, B. Walker, G.-H. Kim, J. Y. Kim, *Nano Energy* **2014**, *7*, 80.
[21] H. X. Dang, K. Wang, M. Ghasemi, M.-C. Tang, M. De Bastiani, E. Aydin, E. Dauzon, D. Barrit, J. Peng, D.-M. Smilgies, S. De Wolf, A. Amassian, *Joule* **2019**, *3*, 1746.
[22] S. Zhang, M.-C. Tang, Y. Fan, R. Li, N. V. Nguyen, K. Zhao, T. D. Anthopoulos, C. A. Hacker, *ACS Appl. Mater. Interfaces* **2020**, *12*, 34402.
[23] X. Liu, M. Chen, Y. Zhang, J. Xia, J. Yin, M. Li, K. G. Brooks, R. Hu, X. Gao, Y.-H. Kim, A. Züttel, J. M. Luther, S. Kinge, Y. Feng, M. K. Nazeeruddin, *Chem. Eng. J.* **2022**, *431*, 133713.
[24] J. Liang, Z. Liu, L. Qiu, Z. Hawash, L. Meng, Z. Wu, Y. Jiang, L. K. Ono, Y. B. Qi, *Adv. Energy Mater.* **2018**, *8*, 1800504.
[25] L. Iagher, L. Etgar, *ACS Energy Lett.* **2018**, *3*, 366.
[26] M. Deepa, M. Salado, L. Calio, S. Kazim, S. M. Shivaprasad, S. Ahmad, *Phys. Chem. Chem. Phys.* **2017**, *19*, 4069.
[27] C. Yi, J. Luo, S. Meloni, A. Boziki, N. Ashari-Astani, C. Grätzel, S. M. Zakeeruddin, U. Röthlisberger, M. Grätzel, *Energy Environ. Sci.* **2016**, *9*, 656.
[28] Z. Li, M. Yang, J.-S. Park, S.-H. Wei, J. J. Berry, K. Zhu, *Chem. Mater.* **2016**, *28*, 284.
[29] M. Kulbak, S. Gupta, N. Kedem, I. Levine, T. Bendikov, G. Hodes, D. Cahen, *J. Phys. Chem. Lett.* **2016**, *7*, 167.
[30] R. Chatterjee, I. M. Pavlovetc, K. Aleshire, G. V. Hartland, M. Kuno, *ACS Energy Lett.* **2018**, *3*, 469.

[31] T. Duong, W. D. A. Rickard, F. Kremer, K. J. Weber, J. Wong-Leung, *J. Phys. Chem. C* **2019**, *123*, 26718.
[32] B. Philippe, M. Saliba, J.-P. Correa-Baena, U. B. Cappel, S.-H. Turren-Cruz, M. Grätzel, A. Hagfeldt, H. Rensmo, *Chem. Mater.* **2017**, *29*, 3589.
[33] G. Pang, X. Lan, R. Li, Z. He, R. Chen, *Nanoscale* **2019**, *11*, 5215.
[34] R. Ohmann, L. K. Ono, H.-S. Kim, H. Lin, M. V. Lee, Y. Li, N.-G. Park, Y. B. Qi, *J. Am. Chem. Soc.* **2015**, *137*, 16049.
[35] J. Hieulle, C. Stecker, R. Ohmann, L. K. Ono, Y. B. Qi, *Small Methods* **2018**, *2*, 1700295.
[36] L. She, M. Liu, D. Zhong, *ACS Nano* **2016**, *10*, 1126.
[37] C. Stecker, K. Liu, J. Hieulle, R. Ohmann, Z. Liu, L. K. Ono, G. Wang, Y. B. Qi, *ACS Nano* **2019**, *13*, 12127.
[38] A. Jamshaid, Z. Guo, J. Hieulle, C. Stecker, R. Ohmann, L. K. Ono, L. Qiu, G. Tong, W. Yin, Y. B. Qi, *Energy Environ. Sci.* **2021**, *14*, 4541.
[39] C. Stecker, Z. Liu, J. Hieulle, S. Zhang, L. K. Ono, G. Wang, Y. B. Qi, *ACS Nano* **2021**, *15*, 14813.
[40] J. Endres, D. A. Egger, M. Kulbak, R. A. Kerner, L. Zhao, S. H. Silver, G. Hodes, B. P. Rand, D. Cahen, L. Kronik, A. Kahn, *J. Phys. Chem. Lett.* **2016**, *7*, 2722.
[41] S. Olthof, K. Meerholz, *Sci. Rep.* **2017**, *7*, 40267.
[42] L. K. Ono, S. Wang, Y. Kato, S. R. Raga, Y. B. Qi, *Energy Environ. Sci.* **2014**, *7*, 3989.
[43] J. Hieulle, X. Wang, C. Stecker, D.-Y. Son, L. Qiu, R. Ohmann, L. K. Ono, A. Mugarza, Y. Yan, Y. B. Qi, *J. Am. Chem. Soc.* **2019**, *141*, 3515.
[44] C. Zhu, X. Niu, Y. Fu, N. Li, C. Hu, Y. Chen, X. He, G. Na, P. Liu, H. Zai, Y. Ge, Y. Lu, X. Ke, Y. Bai, S. Yang, P. Chen, Y. Li, M. Sui, L. Zhang, H. Zhou, Q. Chen, *Nat. Commun.* **2019**, *10*, 815.
[45] M. Goesten, R. Hoffmann, *J. Am. Chem. Soc.* **2018**, *140*, 12996.
[46] M.-C. Tang, H. X. Dang, S. Lee, D. Barrit, R. Munir, K. Wang, R. Li, D.-M. Smilgies, S. De Wolf, D.-Y. Kim, T. D. Anthopoulos, A. Amassian, *Sol. RRL* **2021**, *5*, 2000718.
[47] E. J. Juarez-Perez, L. K. Ono, M. Maeda, Y. Jiang, Z. Hawash, Y. B. Qi, *J. Mater. Chem. A* **2018**, *6*, 9604.
[48] S.-Y. Kim, H. Kang, K. Chang, H.-J. Yoon, *ACS Appl. Mater. Interfaces* **2021**, *13*, 31236.
[49] J. Hieulle, S. Luo, D.-Y. Son, A. Jamshaid, C. Stecker, Z. Liu, G. Na, D. Yang, R. Ohmann, L. K. Ono, L. Zhang, Y. B. Qi, *J. Phys. Chem. Lett.* **2020**, *11*, 818.
[50] H. Yuan, Y. Zhao, J. Duan, Y. Wang, X. Yanga, Q. Tang, *J. Mater. Chem. A* **2018**, *6*, 24324.
[51] X. Hu, X.-F. Jiang, X. Xing, L. Nian, X. Liu, R. Huang, K. Wang, H.-L. Yip, G. Zhou, *Sol. RRL* **2018**, *2*, 1800083.
[52] K. Domanski, B. Roose, T. Matsui, M. Saliba, S.-H. Turren-Cruz, J.-P. Correa-Baena, C. R. Carmona, G. Richardson, J. M. Foster, F. De Angelis, J. M. Ball, A. Petrozza, N. Mine, M. K. Nazeeruddin, W. Tress, M. Grätzel, U. Steiner, A. Hagfeldt, A. Abate, *Energy Environ. Sci.* **2017**, *10*, 604.
[53] M. Bag, L. A. Renna, R. Y. Adhikari, S. Karak, F. Liu, P. M. Lahti, T. P. Russell, M. T. Tuominen, D. Venkataraman, *J. Am. Chem. Soc.* **2015**, *137*, 13130.
[54] S. Meloni, T. Moehl, W. Tress, M. Franckevičius, M. Saliba, Y. H. Lee, P. Gao, M. K. Nazeeruddin, S. M. Zakeeruddin, U. Rothlisberger, M. Graetzel, *Nat. Commun.* **2016**, *7*, 10334.
[55] S. Seo, S. Jeong, C. Bae, N.-G. Park, H. Shin, *Adv. Mater.* **2018**, *30*, 1801010.
[56] M. Saliba, T. Matsui, J.-Y. Seo, K. Domanski, J.-P. Correa-Baena, M. K. Nazeeruddin, S. M. Zakeeruddin, W. Tress, A. Abate, A. Hagfeldt, M. Grätzel, *Energy Environ. Sci.* **2016**, *9*, 1989.
[57] L. Gil-Escrig, C. Momblona, M.-G. La-Placa, P. P. Boix, M. Sessolo, H. J. Bolink, *Adv. Energy Mater.* **2018**, *8*, 1703506,.
[58] M. I. Saidaminov, J. Kim, A. Jain, R. Quintero-Bermudez, H. Tan, G. Long, F. Tan, A. Johnston, Y. Zhao, O. Voznyy, E. H. Sargent, *Nat. Energy* **2018**, *3*, 648.
[59] E. J. Juarez-Perez, R. S. Sanchez, L. Badia, G. Garcia-Belmonte, Y. S. Kang, I. Mora-Sero, J. Bisquert, *J. Phys. Chem. Lett.* **2014**, *5*, 2390.
[60] R. Gottesman, L. Gouda, B. S. Kalanoor, E. Haltzi, S. Tirosh, E. Rosh-Hodesh, Y. Tischler, A. Zaban, C. Quarti, E. Mosconi, F. De Angelis, *J. Phys. Chem. Lett.* **2015**, *6*, 2332.
[61] D. W. De Quilettes, W. Zhang, V. M. Burlakov, D. J. Graham, T. Leijtens, A. Osherov, V. Bulović, H. J. Snaith, D. S. Ginger, S. D. Stranks, *Nat. Commun.* **2016**, *7*, 11683.
[62] W. Zhou, Y. Zhao, X. Zhou, R. Fu, Q. Li, Y. Zhao, K. Liu, D. Yu, Q. Zhao, *J. Phys. Chem. Lett.* **2017**, *8*, 4122.
[63] M. Z. Liu, M. B. Johnston, H. J. Snaith, *Nature* **2013**, *501*, 395.
[64] B. Li, M. Lin, C. Kan, P. Hang, Y. Yao, Z. Hu, Y. Wang, Y. Zhang, W. Zhong, D. Yang, X. Yu, *Sol. RRL* **2022**, *6*, 2200050.
[65] B. Cai, X. Yang, Z. Yu, Y. Liang, Y. Shan, A. Hagfeldt, L. Sun, *J. Power Sources* **2020**, *472*, 228506.
[66] O. Malinkiewicz, A. Yella, Y. H. Lee, G. Minguez Espallargas, M. Grätzel, M. K. Nazeeruddin, H. J. Bolink, *Nat. Photonics* **2014**, *8*, 128.
[67] X. Liu, Q. Han, Y. Liu, C. Xie, C. Yang, D. Niu, Y. Li, H. Wang, L. Xia, Y. Yuan, Y. Gao, *Appl. Phys. Lett.* **2020**, *116*, 253303.
[68] C. Momblona, L. Gil-Escrig, E. Bandiello, E. M. Hutter, M. Sessolo, K. Lederer, J. Blochwitz-Nimoth, H. J. Bolink, *Energy Environ. Sci.* **2016**, *9*, 3456.